Materials Advances

ROYAL SOCIETY OF CHEMISTRY

PAPER

View Article Online
View Journal

Cite this: DOI: 10.1039/d6ma00161k

Optimized grain growth in $CsPbBr_3$ thick films using mist-assisted dissolution–recrystallization for enhanced optoelectronic performance

Monet Brown, Susana Borbon-Rojas, Leunam Fernandez-Izquierdo, Ross Haroldson and Manuel Quevedo-Lopez*

All-inorganic metal halide perovskite (MHP) thick films offer exceptional promise for photodetector applications (visible, UV, X-ray and gamma-ray) due to the stability of inorganic compositions and enhanced radiation absorption of thick-film architectures. However, their performance is often limited, compared to that of their single crystal counterparts, due to small grain sizes and high grain boundary densities which introduce trap states that reduce device efficiency. Here, we introduce a mist-assisted dissolution–recrystallization (MADR) process to enhance the microstructure of blade-coated $CsPbBr_3$ thick films (~200 μm). Applying a $CsPbBr_3$/DMSO mist at controlled concentrations (0.1–0.4 M) followed by low-temperature annealing (60–110 °C) drives a 3.8-fold increase in average grain size from 0.83 ± 0.28 to 3.19 ± 1.57 μm. Under optimal conditions (0.1 M mist, annealing at 85 °C), the MADR-treated film exhibits enlarged grains, reduced trap density, and improved crystallinity, resulting in an ~10^3 order photocurrent enhancement from 1.02 × 10^{-7} to 4.5 × 10^{-4} A cm^{-2} at 5 V under 365 nm illumination (125 mW cm^{-2}). This MADR approach on blade-coated films provides scalable, high-quality perovskite films with low thermal budget and broad substrate compatibility, offering a versatile route for radiation detection and optoelectronic devices.

Received 3rd February 2026,
Accepted 3rd April 2026

DOI: 10.1039/d6ma00161k

rsc.li/materials-advances

Introduction

The exceptional properties of $CsPbBr_3$ such as a wide bandgap (~2.3 eV), high atomic numbers (Cs = 55, Pb = 82, and Br = 35), and a large mobility-lifetime product of 3.2 × 10^{-3} cm^2 V^{-1} have driven substantial interest in optoelectronic applications including sensors, lasers, and photovoltaics.[1–3] The wide band gap reduces the dark current, improving the signal-to-noise ratio, while the high atomic numbers increase the photoelectric absorption.[2,4] These properties have enabled perovskite X-ray detectors to achieve ~200-fold higher sensitivity and ~100-fold lower detection limits than conventional a-Se-based X-ray detectors.[4,5] However, these results are primarily achieved in single crystals of $CsPbBr_3$, which are challenging to scale for commercial manufacturing.[4,6] While scalable methods exist for perovskite thin films (<1 μm), clinically relevant X-ray energies (10 to 100 keV) require 100 to 500 μm thickness for full attenuation.[4,7–9] Similarly, exceptional performance has been reported for visible-UV photodetectors. Bin Yang *et al.* reported solution grown polycrystalline $CsPbBr_3$ thick films with a detectivity of 10^{14} Jones, exceeding single crystals having a reported detectivity of 10^{11} Jones under UV exposure.[10,11] However, such solution submersion growth methods are incompatible with many device architectures.[4] Blade coating has emerged as a scalable fabrication method for perovskite thick films; however, achieving high material quality with controlled grain size remains a critical challenge.[4,12–14]

Kim *et al.* reported that the mobility-lifetime product ($\mu\tau$) of the $MAPbI_3$ blade-coated thick film (1.0 × 10^{-4} cm^2 V^{-1}) is two orders of magnitude lower than that of single-crystal $MAPbI_3$ (1.2 × 10^{-2} cm^2 V^{-1}), highlighting the need to improve performance in blade-coated films.[15,16] Cheng *et al.* addressed this need in $MAPbI_3$ blade-coated thick films using a pore-filling method that enhanced X-ray sensitivity by 5-fold, from 323.86 to 1616.01 μC $Gyair^{-1}$ cm^{-2} under an electric field of 44.44 V mm^{-1}.[6] While this approach has advanced hybrid perovskite thick films, all inorganic perovskite films remain essential for applications requiring long-term operational stability in ambient environments.[17,18] For all-inorganic systems such as $CsPbBr_3$, Shi *et al.* and Gou *et al.* employed dissolution–recrystallization to improve material quality and increase sensitivity *via* a powder "washing" pre-deposition treatment and a surface treatment, respectively.[17,19] These approaches increased the sensitivity from 798 to 14 430 μC $mGyair^{-1}$ cm^{-2}

Department of Material Science & Engineering, University of Texas at Dallas, 2601 N. Floyd Rd, RL10 Richardson, TX 75080, USA.
E-mail: mquevedo@utdallas.edu

at 100 V mm^{-1} (Shi *et al.*) and the methods reported by Gou *et al.* resulted in a 2-fold sensitivity increase.[17,19] Building on these strategies, this work introduces a novel mist-assisted dissolution–recrystallization technique to increase bulk grain size and crystallite size in all-inorganic perovskite thick films ($\sim$200 μm).

Leveraging crystallization kinetics to control grain size and crystallite size in blade-coated $CsPbBr_3$ thick films, this work systematically decouples the processing conditions that govern dissolution–recrystallization dynamics, establishing a framework for enhancing film quality and device-relevant optoelectronic properties at low processing temperatures. Grain size refers to the dimensions of individual particles observed under a microscope, whereas crystallite size represents the coherent scattering domain size determined from XRD analysis. This method employs a DMSO-based mist solution containing dissolved $CsPbBr_3$ (0.1 M, 0.2 M, or 0.4 M) applied to blade-coated $CsPbBr_3$ thick films. The mist penetrates the bulk of the film and partially dissolves the perovskite, creating a saturated or supersaturated environment. Upon annealing at controlled temperatures (60, 85, or 110 °C), the system undergoes Ostwald ripening within the metastable zone, where grain coarsening, distinct from nucleation and crystal growth, proceeds *via* surface-energy-driven material transport from smaller grains to larger grains.[20,21] This mist-assisted dissolution–recrystallization (MADR) technique achieves substantial grain size increases, with optimal conditions (0.1 M, 85 °C) yielding grain sizes of 3.19 ± 1.57 μm compared to 0.83 ± 0.28 μm in the as-deposited films. Correspondingly, the photocurrent response, a key metric for evaluating charge collection efficiency in photodetector applications, increases by over three orders of magnitude, from 1.02 × 10^{-7} to 4.5 × 10^{-4} A cm^{-2} at 5 V in a Pt/$CsPbBr_3$/Pt planar device illuminated with a 365 nm LED at 125 mW cm^{-2}. These results demonstrate that controlled temperature-concentration dynamics enable targeted grain coarsening in $CsPbBr_3$, substantially improving optoelectronic performance. This solution-based approach is generalizable to a diversity of perovskite systems and can be applied iteratively to further improve performance enhancements, offering a scalable pathway toward high-efficiency thick film perovskite optoelectronic devices and radiation detectors.

Results

While $CsPbBr_3$ single-crystals and thin films have been reported to exhibit excellent optoelectronic properties, thick films (100–500 μm) required for commercially relevant high-energy photon applications often struggle to achieve large grains, high crystallinity, and high carrier mobility.[4] Overcoming these processing challenges is therefore essential for translating the intrinsic properties of MHPs into practical device performance.

Fig. 1(a) and (b) show the cross-sectional SEM images of the as-deposited $CsPbBr_3$ thick film fabricated by blade coating. The as-deposited film exhibits a highly porous microstructure with small grains, characteristic of blade-coated films.[4,13] Fig. 1(c) shows the grain size distribution of the as-deposited $CsPbBr_3$ film, with an average grain size of 0.83 ± 0.28 μm. Such a small grain-to-thickness ratio and high porosity commonly lead to reduced device performance.[4,19] Subsequently, MADR treatment was applied to improve film quality. We systematically investigated the effects of annealing temperature and mist concentration on grain morphology and crystallite size. The DMSO/$CsPbBr_3$ mist induces partial dissolution when applied to the porous, fine-grained as-deposited film and subsequent annealing promotes grain growth that increases film density, grain size, and crystallite size.

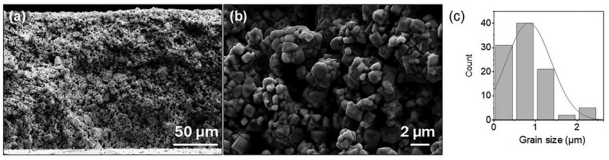

Fig. 1 (a) and (b) SEM cross-sectional images of the as-deposited $CsPbBr_3$ 200 μm thick film. (c) Grain size distribution of the as-deposited $CsPbBr_3$ 200 μm thick film. The average grain size of 50 grains is 0.83 ± 0.28 μm.

Impact of mist concentration and annealing temperature on $CsPbBr_3$ film microstructure

To promote grain growth, MADR was performed on the as-deposited $CsPbBr_3$ thick films. Exposure to pure DMSO mist caused nonuniform grain size distribution (Fig. S1), whereas incorporating $CsPbBr_3$ into the mist enabled more homogeneous solvent–film interactions and improved film uniformity. A DMSO/$CsPbBr_3$ mist solution was applied at concentrations of 0.1 M, 0.2 M, and 0.4 M due to the solubility limit of $CsPbBr_3$ in DMSO (0.5 M).[22] Cross-sectional SEM images of films treated at each mist concentration are shown in Fig. 2. Low mist concentration (0.1 M) produced larger grains (1.91–3.19 μm), attributed to more uncoordinated DMSO molecules that promote Ostwald ripening.[20,21] Conversely, at higher mist concentrations (0.4 M), there is limited dissolution, yielding smaller grains (0.97–1.52 μm).[11,23–25] Recrystallization temperatures of 60, 85, and 110 °C were selected to probe solvent-assisted growth kinetics below the 189 °C boiling point of DMSO (Fig. 2). Annealing at 85 °C produced the largest grain size increase (1.45–3.19 μm). At 60 °C, insufficient thermal energy limits grain coarsening (0.97–2.09 μm), whereas at 110 °C, faster DMSO evaporation suppresses further growth (1.52–1.91 μm). Grain sizes and corresponding standard deviations are summarized in Table S1.

These observations are consistent with established crystallization kinetics models: within the solubility and supersolubility boundaries (the metastable zone), Ostwald ripening is the dominant mechanism; whereas above the supersolubility boundary (the labile region), supersaturation promotes spontaneous crystallization and suppresses ripening.[20,21,23,24] Under optimal conditions, average grain size increased from 0.83 ± 0.28 μm in the as-deposited film to 3.19 ± 1.57 μm with 0.1 M mist and annealing at 85 °C, indicating that this condition lies

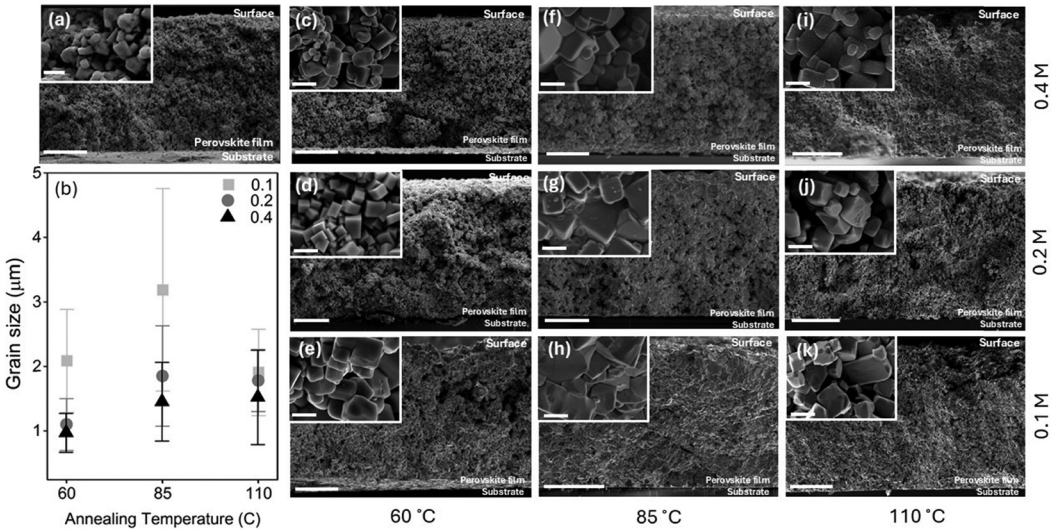

Fig. 2 (a) SEM cross-sectional images of the as-deposited bladed-coated $CsPbBr_3$ film and (b) grain size distribution of mist-assisted dissolved and recrystallized $CsPbBr_3$ films. The films were annealed at (c)–(e) 60 °C, (f)–(h) 85 °C, and (i)–(k) 110 °C using a mist solution of DMSO and $CsPbBr_3$ powder at concentrations of 0.1 M (bottom row), 0.2 M (middle row), and 0.4 M (top row). All scale bars represent 50 μm and 2 μm in insets.

near the center of the metastable zone where ripening is most pronounced.[23,26] These parameters collectively define useful boundaries for distinguishing the metastable and labile regions. XRD analysis, discussed in the next section, was conducted to validate the proposed mechanism by quantifying crystallite size evolution. Larger crystallite sizes at higher mist concentrations corroborate the SEM results and crystallization kinetics described above.[23]

Impact of mist concentration and annealing temperature on $CsPbBr_3$ crystallinity

The effects of mist solution concentration and annealing temperature on film composition were evaluated by X-ray diffraction (Fig. 3). At moderate mist concentration (0.2 M), secondary Cs–Pb–Br phases formed at 60 °C, whereas a higher mist concentration (0.4 M) induces secondary phase formation at both 60 and 85 °C. At 60 °C, the diffraction peaks at 11.6, 12.5, 30.9, and 31 2θ (degrees) correspond to tetragonal $CsPb_2Br_5$ and rhombohedral Cs_4PbBr_6 (Fig. S2). Peaks associated with rhombohedral Cs_4PbBr_6 appeared in 0.4 M films annealed at 85 °C (Fig. S3). No reflections associated with secondary phases were observed at 110 °C. Phase compositions are summarized in Table S1.

The XRD data were further analyzed to estimate crystallite size using the Scherrer equation.[27] As shown in Fig. 3(d), MADR treatment at 85 °C with 0.1 M mist concentration increased the crystallite size to 44.22 ± 10.81 nm from 40.92 ± 2.66 nm in the as-deposited film. At 110 °C with 0.4 M mist concentration, the crystallite size increased to 125.48 ± 9.56 nm, the maximum observed value. Crystal growth occurs *via* the expansion of a single crystalline domain through coalescence of domains with coherent planes, a process favored by the high supersaturation conditions that bring crystallites into proximity.[28] Grain growth results from the aggregation of multiple domains with incoherent planes. Correlation of XRD and SEM results shows that variations in mist concentration and annealing temperature

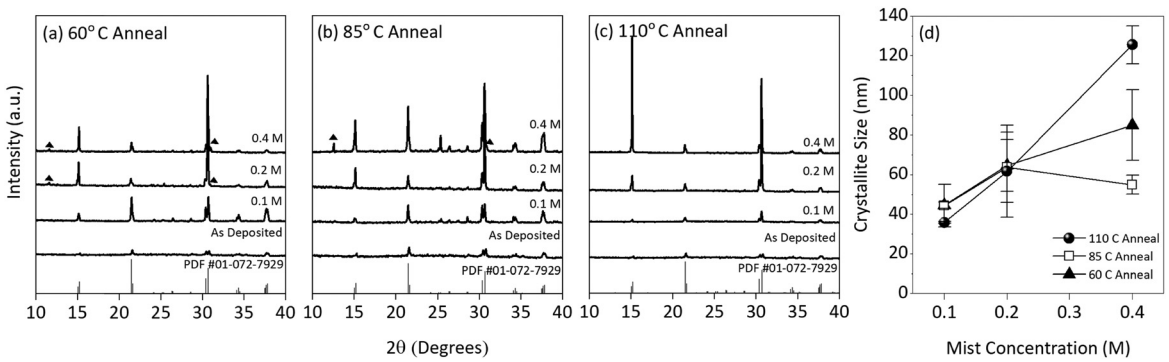

Fig. 3 X-ray diffraction patterns of the as-deposited and treated films at each mist solution concentration (0.1, 0.2 and 0.4 M) and annealing at (a) 60 °C, (b) 85 °C, (c) 110 °C are presented. Peaks that do not correspond to orthorhombic $CsPbBr_3$ are accompanied by a triangle with tetragonal $CsPb_2Br_5$ and rhombohedral Cs_4PbBr_6 present at 60 °C and rhombohedral Cs_4PbBr_6 at 85 °C. (d) Crystallite size as a function of mist solution concentration.

modulate the balance between these mechanisms, determining which mechanism dominates under specific MADR conditions.

The combined SEM and XRD results are interpreted within a thermodynamic–kinetic model for crystallization. At low mist concentrations, the system lies within the metastable region, where abundant uncoordinated DMSO molecules promote grain coarsening through Ostwald ripening, resulting in larger grain sizes but minimal change in crystallite size.[21,23,26] Increasing mist concentration shifts the system toward the labile region, where reduced DMSO availability limits solvent-induced ripening, and unstable supersaturation promotes spontaneous crystallization, producing smaller grains with a larger crystallite size.[21,23,26] Annealing temperature further modulates these effects as DMSO, with a boiling point of 189 °C, exhibits slow evaporation kinetics at 60 °C that progressively increase up to 110 °C. Therefore, SEM grain size peaks at a moderate temperature of 85 °C where thermal energy is sufficient for grain coarsening, while XRD crystallite size increases with temperature as faster solvent evaporation at 110 °C favors crystalline ordering and lacks the solvent availability for grain growth (Fig. S4). The resulting microstructure is therefore governed by the coupled effects of supersaturation and temperature, as illustrated in Fig. 4.

Impact of grain growth and crystallite size on optoelectronic properties

The recrystallized film with the largest grains and lowest porosity (0.1 M, 85 °C) was selected, as grain boundaries and pores act as primary barriers to charge transport in polycrystalline films.[16,29] This film was compared to the as deposited film and evaluated using steady-state photoluminescence (PL). As shown in Fig. 5, two emission bands appear: a primary $CsPbBr_3$ band at 525 nm and a secondary band near 540 nm, attributed to defect-related emission in $CsPbBr_3$.[10] Band-fitting results are shown in Fig. 5(b) and (c). The PL spectra were fitted with a mixed Gaussian–Lorentzian function in OriginPro 2025, yielding reduced chi-squared values of $<1 \times 10^{-5}$ (see Table S2). The recrystallized film exhibits reduced relative intensity in the 540 nm defect-related band and enhanced emission at 525 nm, indicating that MADR treatment significantly reduces defect states. Furthermore, the PL emission of the 0.2 M film deposited at 60 °C, which contains secondary phases ($CsPb_2Br_5$ and Cs_4PbBr_6) as identified by XRD, is blue-shifted relative to the 0.2 M films deposited at 85 °C and 110 °C, which consist of phase-pure $CsPbBr_3$, consistent with prior reports of blue-shifted emission in Cs–Pb–Br systems containing Cs_4PbBr_6 secondary phases (see Fig. S5).[30]

The photocurrent response for the planar Pt/$CsPbBr_3$/Pt devices fabricated using the as-deposited film and selected recrystallized film was evaluated using a 365 nm light source (from dark to 125 mW cm^{-2}; Fig. 6a and b). The MADR-treated film shows a higher photocurrent, consistent with reduced defect density from steady-state PL. MADR-induced grain coarsening reduces grain boundary density and passivates trap states, eliminating *I–V* asymmetry observed in the as-deposited film.[31,32] Fig. 6(c) shows the photocurrent response at 5 V as a function of illumination intensity. At 5 V bias, the as-deposited film exhibits 1.02×10^{-7} A cm^{-2}, whereas the recrystallized film shows a 440-fold enhancement to 4.5×10^{-4} A cm^{-2} (Fig. 5c). The sheet conductance of the as-deposited film was determined to be 1.42×10^{-11} S, increasing to 2.72×10^{-10} S following MADR treatment, indirectly indicating enhanced charge transport in the recrystallized film (see Section S2).

Current–time measurements under a 125 mW cm^{-2} illumination intensity results in a photocurrent response of 9.3×10^{-8} A cm^{-2} in the as-deposited film, while the recrystallized film reaches 3.8×10^{-4} A cm^{-2}. The recrystallized film also exhibits rise and decay times of <27.4 ms and <4.6 ms, respectively (Fig. 7a and b). As shown in Fig. 7(c) and (d), both photocurrent and response speed improve with increasing illumination intensity (2.2 to 125 mW cm^{-2}). A higher light intensity generates more electron–hole pairs and progressively fills trap states, reducing the density of the available trapping sites that would otherwise delay charge collection.[33]

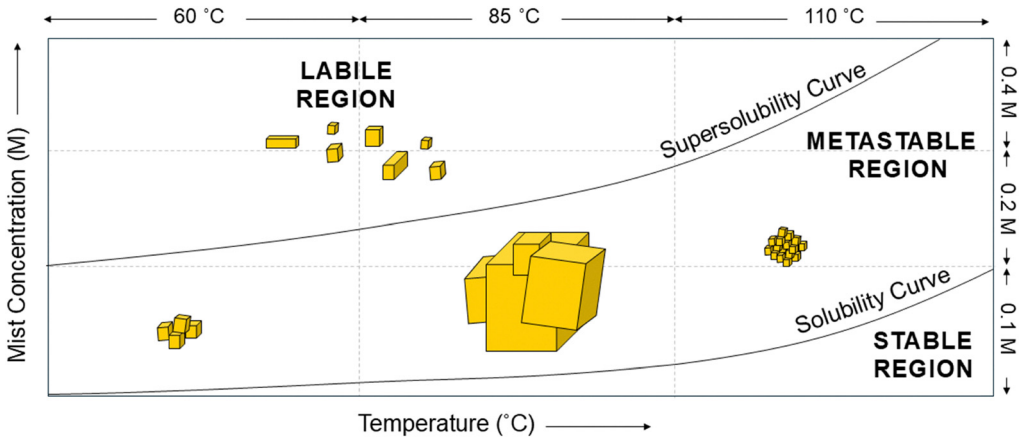

Fig. 4 Schematic showing grain growth and crystal growth as a function of mist concentration and annealing temperature in $CsPbBr_3$ films as an adaptation of classic crystallization models.[23,24] Optimal grain growth occurs at moderate temperature (85 °C) and low concentration (0.1 M) within the metastable region. Higher concentrations promote rapid crystallization, yielding smaller grains with larger crystallite sizes.

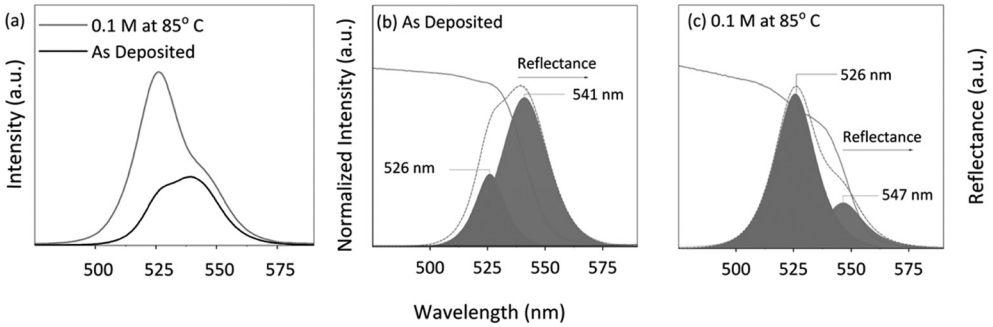

Fig. 5 (a) Photoluminescence spectroscopy of the as-deposited film and recrystallized film saturated with a 0.1 M solution and annealed at 85 °C. Figures (b) and (c) show the fitting of the PL spectra.

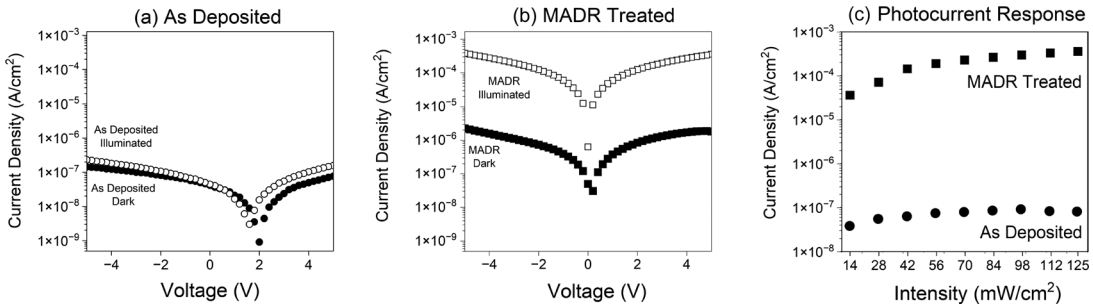

Fig. 6 IV characterization of (a) the as-deposited film compared to (b) the film recrystallized with a 0.1 M solution at 85 °C under dark conditions and illuminated at 125 mW cm^{-2} and (c) the photocurrent response of the as-deposited film and the recrystallized film across illumination intensities at a 5 V bias.

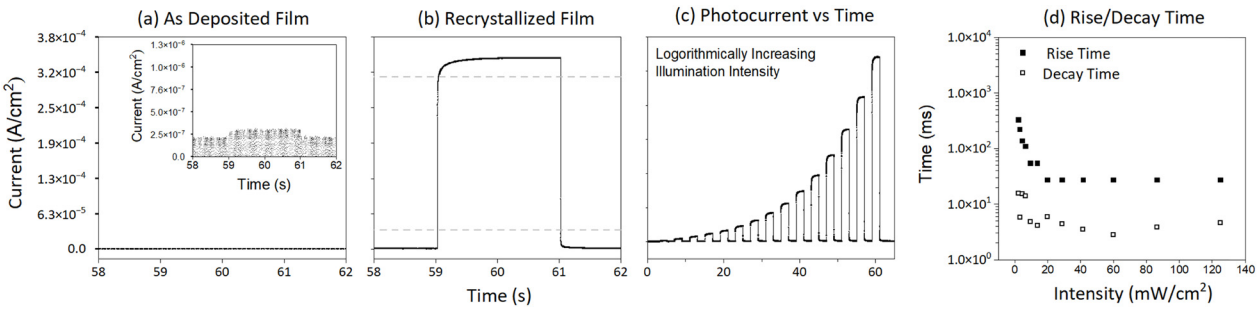

Fig. 7 Time–current response of (a) the as-deposited film and (b) the film recrystallized with a 0.1 M solution at 85 °C. (c) The time–current response of the recrystallized film was measured with logarithmically spaced illumination intensity from 0.03 mW cm^{-2} to 125 mW cm^{-2}. (d) Rise and decay times of the recrystallized sample across logarithmically spaced illumination intensities from 2.2 mW cm^{-2} to 125 mW cm^{-2}. Measurements were made under 5 V bias with a 365 nm light source.

The as-deposited film exhibited a responsivity of 1.07×10^{-5} A W^{-1} and a specific detectivity of 3.58×10^{6} Jones. Following MADR treatment, the responsivity and detectivity increased to 3.59×10^{-3} A W^{-1} and 5.04×10^{9} Jones, respectively, demonstrating a significant enhancement in photodetector performance upon recrystallization (see Section S3). To assess ambient stability, the MADR-treated film was stored unencapsulated between 20 and 30 °C and 45 and 65% RH for 6 months, after which it retained a sustained photocurrent response exceeding 10 continuous minutes, demonstrating reasonable long-term operational stability (see Fig. S6).

Hot-pressed $CsPbBr_3$ pellets fabricated from mechanochemically synthesized ball-milled powder exhibit a comparable grain size ($\sim$0.4 μm^2) and a higher absolute photocurrent response ($\sim 10^{-7}$ A) relative to the as-deposited film in this work (0.83 ± 0.28 μm and 9×10^{-11} A).[3] MADR treatment induces a pronounced increase in photocurrent from the low response of the as deposited film (9×10^{-11} A, corresponding to 1.02×10^{-7} A cm^{-2}) to a photocurrent density of 4.5×10^{-4} A cm^{-2} under identical measurement conditions. Solution-grown polycrystalline films, such as those reported by Yang *et al.*, show higher photocurrent densities

Table 1 Comparison of $CsPbBr_3$ thick films based on the fabrication method and their properties (grain size, thickness, processing temperature, and photocurrent response)

Fabrication method	Average grain size (μm^2)	Thickness (μm)	Processing temperature (°C)	Photocurrent (A)	Photocurrent density (A cm^{-2})	Ref.
Mechanochemical and hot pressing	~0.4	400–700	100	$\sim 10^{-8}$	—	3
Blade coated	0.83 ± 0.28	~200	85	9.0×10^{-11}	1.02×10^{-7}	This work
Dissolution–recrystallization	3.19 ± 1.57	~200	85	3.75×10^{-7}	4.5×10^{-4}	This work
Solution grown microcrystals	—	~200	140	6.0×10^{-3}	1.2×10^{-2}	10

(1.2×10^{-2} A cm^{-2}, calculated from the reported data), indicating the upper performance limits achievable with solution grown highly crystalline thick films.[10]

MADR-treated blade-coated films nonetheless exhibit a competitive photocurrent response, with further improvements anticipated through iterative dissolution–recrystallization cycles. When considered alongside scalability, low thermal budget, and broad substrate compatibility, this approach represents a feasible route to large-scale perovskite thick film fabrication for optoelectronic applications. A comparison of these fabrication techniques is summarized in Table 1.

Experimental

The schematic of the MADR method for bulk recrystallization of blade-coated $CsPbBr_3$ films is shown in Fig. 8. In this method, CsBr and $PbBr_2$ precursors are ball-milled to synthesize $CsPbBr_3$ powder. The $CsPbBr_3$ powder is then used to prepare a slurry to deposit a 200 μm thick film onto a glass substrate using the conventional Dr. Blade method. After film deposition, the $CsPbBr_3$ films are partially dissolved using a $CsPbBr_3$/DMSO mist solution at concentrations of 0.1, 0.2 and 0.4 M and then annealed at either 60, 85 or 110 °C for 30 minutes. Platinum contacts were used for the fabrication of the devices used for optoelectronic characterization.

Materials

Cesium bromide (CsBr, 99.9%) was obtained from Alfa-Aesar and lead(II) bromide ($PbBr_2$, 99.99%) and dimethyl sulfoxide (DMSO) from Sigma-Aldrich. For the ball milling process, stainless-steel balls (2 mm), milling jars, and a high-energy vertical planetary ball mill were acquired from MSE Supplies LLC.

Blade-coated films

Glass substrates underwent sequential 10-minute sonication steps in acetone, isopropyl alcohol, deionized water, and methanol. After drying with nitrogen, the substrates were annealed at 115 °C for 2 minutes and cleaned with oxygen-based reactive ion etching (RIE) for 10 minutes to remove organic residues and moisture. $CsPbBr_3$ films were then deposited on the glass by blade coating. The $CsPbBr_3$ powder precursors were synthesized *via* mechanochemical ball milling following a previously reported method.[34] The resulting $CsPbBr_3$ powder was sieved through a 0.2 μm pore-sized mesh to prevent agglomerated particles in the blade coating slurry. To prepare the slurry for blade coating, 1.5 mg of ethyl cellulose was dissolved in a mixture of 0.3 mL of *n*–*n*-dodecane and 0.7 mL of α-terpineol by sonicating for 20 minutes. The slurry is then prepared using 30 μL of the prepared solution per 100 mg of $CsPbBr_3$ ball milled powder. This slurry was then used to blade-coat $CsPbBr_3$ films onto a glass substrate at 2 mm s^{-1} at room temperature (Fig. 8c). The blade-coated films were annealed at 85 °C for 10 minutes at a heating rate of 1 °C min^{-1}.

Mist-assisted dissolution–recrystallization (MADR)

Next, the film was exposed to a mist solution for dissolution–recrystallization. The mist solution was prepared by dissolving ball-milled $CsPbBr_3$ powder in dimethyl sulfoxide (DMSO) at 0.1, 0.2, and 0.4 M, followed by stirring for 18 hours at room temperature. Then 5 mL of the mist solution was applied to 200 μm thick films through a 0.5 mm nozzle propelled by nitrogen at 50 psi with a sample-to-nozzle distance of 15 inches, as shown in Fig. 8c. Then annealing was performed for 30 minutes at either 60, 85, or 110 °C at a ramp rate of 1 °C min^{-1} (Fig. 8e).

Device fabrication

Devices were fabricated by depositing platinum contacts (7×10^{-4} cm^2, 2×10^{-2} cm apart with an active area of 2×10^{-4} cm^2) onto the surface of $CsPbBr_3$ thick films *via* e-beam physical vapor deposition to fabricate a planar Pt/$CsPbBr_3$/Pt architecture.

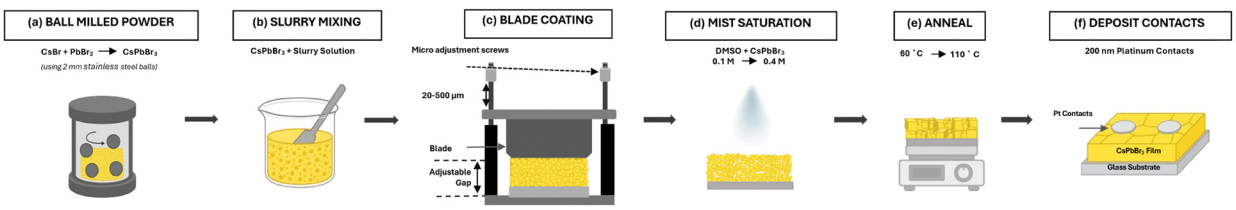

Fig. 8 Experimental setup for: (a) ball milling of perovskite powder, (b) slurry preparation, (c) film deposition by blade coating, (d) film treatment with a mist solution, (e) annealing to facilitate recrystallization, and (f) deposition of platinum contacts (E-beam evaporation).

Material and device characterization studies

Scanning electron microscopy (SEM) images of the polycrystalline blade-coated thick films were obtained using a Zeiss Sigma 500VP. Cross-sectional images were acquired by cleaving the glass substrate-supported films. The average grain size was measured using ImageJ software.[35] X-ray diffraction (XRD) patterns were obtained using a Rigaku SmartLab X-ray diffraction system equipped with a copper CuKα radiation source (λ = 1.5406 Å) at a current of 30 mA and a voltage of 40 kV and the crystallite size was calculated using the Scherer equation.[27] UV–Vis measurements were performed using an Agilent UV–Vis–NIR spectrophotometer with a mercury arc lamp and multi-angle reflection (R) capability. Steady state photoluminescence (PL) was measured with a 405 nm light emitting diode (LED), a 0.8 mm aperture, and an output of 100 mW cm^{-2}. Photocurrent response was measured using a 365 nm LED modulated from dark to 125 mW cm^{-2}. Current–voltage characteristics of the planar Pt/$CsPbBr_3$/Pt device were measured in a probe station with a Keithley 4200 system.

Conclusion

This study demonstrates a low temperature, mist-assisted dissolution–recrystallization (MADR) process for scalable control of microstructure in blade-coated $CsPbBr_3$ thick films. At low mist concentrations, partial dissolution promotes grain coarsening through Ostwald ripening, yielding larger grains. Higher concentrations reduce dissolution, resulting in smaller grains. Annealing temperature modulates these effects: insufficient heating limits ripening, while excessive heating accelerates solvent evaporation and quenches grain growth. Careful control of mist concentration and annealing temperature enables precise grain and crystallite size tuning, significantly improving the photocurrent response by reducing defect density. This approach offers a pathway for engineering high-quality perovskite thick films for X-ray detection, photodetectors, and other applications requiring high-performance, large-area devices.

Author contributions

Monet Brown: conceptualization, data curation, formal analysis, investigation, methodology, visualization, writing – original draft, and writing – review and editing. Susana Borbon-Rojas: methodology and writing – review and editing. Leunam Fernandez-Izquierdo: validation and writing – review and editing. Ross Haroldson: data curation. Manuel Quevedo-Lopez: conceptualization, funding acquisition, project administration, resources, supervision, validation, and writing – review and editing.

Conflicts of interest

There are no conflicts to declare.

Data availability

The data supporting this article have been included as part of the supplementary information (SI). Supplementary information: Fig. S1–S6, Tables S1, S2 and Section S1–S3. See DOI: https://doi.org/10.1039/d6ma00161k.

Acknowledgements

The authors would like to express their gratitude to the University of Texas at Dallas and The Texas Instruments Chair in Nanoelectronics for partial financial support.

References

1 Y. Hua, X. Sun, X. Li, F. Cui, Z. Yue, J. Liu, H. Liu, G. Zhang and X. Tao, *J. Mater. Chem. C*, 2023, **11**, 9153–9160.
2 N. Grundmanis, A. Sarakovskis, A. Lupilov, V. Gostilo, A. Owens and K. Pudzs, *Nucl. Instrum. Methods Phys. Res., Sect. A*, 2025, **1073**, 170305.
3 M. Sotelo-Lerma, L. Fernandez-Izquierdo, M. A. Ruiz-Molina, I. Borges-Doren, R. Haroldson and M. Quevedo-Lopez, *Materials*, 2024, **17**, 5123.
4 Y. Haruta, M. Kawakami, Y. Nakano, S. Kundu, S. Wada, T. Ikenoue, M. Miyake, T. Hirato and M. I. Saidaminov, *Chem. Mater.*, 2022, **34**, 5323–5333.
5 J. Peng, C. Q. Xia, Y. Xu, R. Li, L. Cui, J. K. Clegg, L. M. Herz, M. B. Johnston and Q. Lin, *Nat. Commun.*, 2021, **12**, 1531.
6 J. Cheng, C. Xue, M. Yang, X. Wang, Z. Xu, N. Li, X. Zhang, X. Feng, X. Liu, Y. Liu, S. F. Liu and Z. Yang, *ACS Appl. Mater. Interfaces*, 2024, **16**, 36649–36657.
7 T. Zou, B. Xiang, Y. Xu, Y. Wang, C. Liu, J. Chen, K. Wang, Q. Dai, S. Zhang, Y.-Y. Noh and H. Zhou, *IEEE J. Electron Devices Soc.*, 2021, **9**, 96–101.
8 S. V. N. Pammi, V.-D. Tran, R. Maddaka, J.-H. Eom, J. S. Jung, H.-M. Jeong, M.-D. Kim, V. Pecunia and S. G. Yoon, *Adv. Opt. Mater.*, 2020, **8**, 2000845.
9 S. V. N. Pammi, H.-W. Lee, J.-H. Eom and S.-G. Yoon, *ACS Appl. Energy Mater.*, 2018, **1**, 3301–3312.
10 B. Yang, F. Zhang, J. Chen, S. Yang, X. Xia, T. Pullerits, W. Deng and K. Han, *Adv. Mater.*, 2017, **29**, 1703758.
11 Z. Zhang, H. Li, H. Di, D. Liu, W. Jiang, J. Ren, Z. Fan, F. Liao, L. Lei, G. Li, Y. Xiong and Y. Zhao, *ACS Appl. Electron. Mater.*, 2023, **5**, 388–396.
12 K.-W. Huang, M.-H. Li, Y.-T. Chen, Z.-X. Wen, C.-F. Lin and P. Chen, *J. Mater. Chem. C*, 2024, **12**, 1533–1542.
13 M. Xia, Z. Song, H. Wu, X. Du, X. He, J. Pang, H. Luo, L. Jin, G. Li, G. Niu and J. Tang, *Adv. Funct. Mater.*, 2022, **32**, 2110729.
14 B. Yang, W. Pan, H. Wu, G. Niu, J.-H. Yuan, K.-H. Xue, L. Yin, X. Du, X.-S. Miao, X. Yang, Q. Xie and J. Tang, *Nat. Commun.*, 2019, **10**, 1989.
15 H. Wei, Y. Fang, P. Mulligan, W. Chuirazzi, H.-H. Fang, C. Wang, B. R. Ecker, Y. Gao, M. A. Loi, L. Cao and J. Huang, *Nat. Photonics*, 2016, **10**, 333–339.

16 Y. C. Kim, K. H. Kim, D.-Y. Son, D.-N. Jeong, J.-Y. Seo, Y. S. Choi, I. T. Han, S. Y. Lee and N.-G. Park, *Nature*, 2017, **550**, 87–91.
17 Z. Gou, S. Huanglong, W. Ke, H. Sun, H. Tian, X. Gao, X. Zhu, D. Yang and P. Wangyang, *Phys. Status Solidi RRL*, 2019, **13**, 1900094.
18 A. Choubey, N. Perumal, S. Narendhiran, S. P. Muthu and R. Perumalsamy, *Int. J. Energy Res.*, 2022, **46**, 9310–9322.
19 T. Shi, W. Liu, J. Zhu, X. Fan, Z. Zhang, X. He, R. He, J. Wang, K. Chen, Y. Ge, X. Sun, Y. Liu, P. K. Chu and X.-F. Yu, *Nano Res.*, 2023, **16**, 9983–9989.
20 X. Cao, L. Zhi, Y. Li, F. Fang, X. Cui, L. Ci, K. Ding and J. Wei, *ACS Appl. Energy Mater.*, 2018, **1**, 868–875.
21 T. Vetter, M. Iggland, D. R. Ochsenbein, F. S. Hänseler and M. Mazzotti, *Cryst. Growth Des.*, 2013, **13**, 4890–4905.
22 X. Cao, G. Zhang, L. Hao, X. Ding, T. Dong, X. Li, Q. Zeng, X. He, Y. Jia and J. Wei, *J. Alloys Compd.*, 2022, **919**, 165722.
23 Y. Zhang, in *Modelling of Chemical Process Systems*, ed. S. A. Imtiaz, Elsevier, 2023, pp. 181–202.
24 J.-P. Duroudier, in *Crystallization and Crystallizers*, ed. J.-P. Duroudier, Elsevier, 2016, pp. 39–78.
25 S. Kim and A. S. Myerson, *Ind. Eng. Chem. Res.*, 1996, **35**, 1078–1084.
26 M. A. Behrens, A. Franzén, S. Carlert, U. Skantze, L. Lindfors and U. Olsson, *Soft Matter*, 2025, **21**, 2349–2354.
27 P. Scherrer, *Math. Phys.*, 1918, **2**, 98–100.
28 S. Li, Y. Xiao, R. Su, W. Xu, D. Luo, P. Huang, L. Dai, P. Chen, P. Caprioglio, K. A. Elmestekawy, M. Dubajic, C. Chosy, J. Hu, I. Habib, A. Dasgupta, D. Guo, Y. Boeije, S. J. Zelewski, Z. Lu, T. Huang, Q. Li, J. Wang, H. Yan, H.-H. Chen, C. Li, B. A. I. Lewis, D. Wang, J. Wu, L. Zhao, B. Han, J. Wang, L. M. Herz, J. R. Durrant, K. S. Novoselov, Z.-H. Lu, Q. Gong, S. D. Stranks, H. J. Snaith and R. Zhu, *Nature*, 2024, **635**, 874–881.
29 T. Meier, H. Bässler and A. Köhler, *Adv. Opt. Mater.*, 2021, **9**, 2100115.
30 J. Li, H. Zhang, S. Wang, D. Long, M. Li, D. Wang and T. Zhang, *Materials*, 2018, **11**, 717.
31 W. Xu, T. Du, M. Sachs, T. J. Macdonald, G. Min, L. Mohan, K. Stewart, C.-T. Lin, J. Wu, R. Pacalaj, S. A. Haque, M. A. McLachlan and J. R. Durrant, *Cell Rep. Phys. Sci.*, 2022, **3**, 100890.
32 A. B. Andrabi and A. T. Mallajosyula, *Sol. Energy*, 2023, **264**, 112020.
33 J. Pan, Z. Chen, T. Zhang, B. Hu, H. Ning, Z. Meng, Z. Su, D. Nodari, W. Xu, G. Min, M. Chen, X. Liu, N. Gasparini, S. A. Haque, P. R. F. Barnes, F. Gao and A. A. Bakulin, *Nat. Commun.*, 2023, **14**, 8000.
34 M. Shekarnoush, L. Fernandez-Izquierdo, F. S. Aguirre-Tostado, Z. H. Shamsi and M. A. Quevedo-Lopez, *Chem. Mater.*, 2023, **35**(21), DOI: 10.1021/acs.chemmater.3c01440.
35 R. Wayne, Image J (version 1.54p) National Institutes of Health and the Laboratory for Optical and Computational Instrumentation, 2025.